Science Advances

AAAS

advances.sciencemag.org/cgi/content/full/4/2/eaar2250/DC1

Supplementary Materials for

Current-induced magnetization switching using an electrically insulating spin-torque generator

Hongyu An, Takeo Ohno, Yusuke Kanno, Yuito Kageyama, Yasuaki Monnai, Hideyuki Maki, Ji Shi, Kazuya Ando

Published 23 February 2018, *Sci. Adv.* **4**, eaar2250 (2018)
DOI: 10.1126/sciadv.aar2250

This PDF file includes:

section S1. Materials' characterization

To investigate the microstructure of the Pt(O) films used in the present study, X-ray diffraction (XRD) and X-ray reflectivity (XRR) measurements were conducted with a Bruker D8 Discover diffractometer by applying Cu K_α radiation. Single Pt(O) layer films were fabricated by changing oxygen flow Q for the measurements. As shown in fig. S1A, when no oxygen is incorporated, a strong (111) peak is observed, indicating a highly (111)-oriented texture in the Pt film. By increasing Q to 8%, the Pt (111) peak drastically decreases. By further increasing Q, no peak can be observed, which indicates that the Pt(O) films change to amorphous structure by the incorporation of oxygen. Furthermore, from the XRR profiles (see fig. S1B), it can be confirmed that the decay beginning angle becomes smaller as Q increases, which indicates the density of the Pt(O) films decreases with the increase of Q. By fitting the measured XRR profiles using the Bruker LEPTOS software with the Levenberg-Marquardt method, we have obtained the Q dependence of the Pt(O) density and plotted it in fig. S1C. Unambiguously, the Pt(O) density decreases with Q. It has been reported that the densities of bulk PtO and PtO_2 are 14 g/cm^3 and 11 g/cm^3, respectively (*20*), as plotted by the dashed lines in fig. S1C. From the magnitude change of the density, it can be interpreted that as Q increases from 0 to 35%, the composition of the films changes from Pt to PtO, and then changes to PtO_2.

section S2. Second harmonic measurement of the AHE resistance

In order to confirm the existence of the damping-like torque in the MgO/CoTb/Pt(O) heterostructure with $Q = 16\%$, second harmonic measurements of the anomalous Hall effect (AHE) resistance were carried out (*10*). In the measurement, an ac current with a frequency of 507.32 Hz was applied in the longitudinal direction of the device and a lock-in amplifier was used to measure the signal. A second harmonic AHE resistance $R_{\mathrm{H}}^{2\omega}$ can be generated when the current induced alternating damping-like effective field $\mu_0 H_{\mathrm{DL}}$ drives the oscillation of the magnetization around its equilibrium state. As shown in fig. S2A, by sweeping an external magnetic field $\mu_0 H_x$ in the longitudinal direction, the variation of $R_{\mathrm{H}}^{2\omega}$ was observed. We measured the $R_{\mathrm{H}}^{2\omega}$ by changing the ac current and fitted the curves in the ranges where the external magnetic field is larger than the saturation field (see fig. S2B) using

$$R_{\mathrm{H}}^{2\omega} = -\frac{1}{2}\frac{R_{\mathrm{H}}\mu_0 H_{\mathrm{DL}}}{|\mu_0 H_x| - \mu_0 H_{\mathrm{K}}} \tag{1}$$

where R_{H} and $\mu_0 H_{\mathrm{K}}$ are the perpendicular saturation AHE resistance and the saturation magnetic field, respectively (*10*). Here, we neglect the planar Hall effect (PHE) contribution to the second harmonic Hall resistance, since the PHE resistance is negligibly small compared to the AHE resistance in the MgO/CoTb/Pt(O) heterostructure. The transverse resistance change ΔR_{PHE} due to the PHE is shown in fig. S3, where $\Delta R_{\mathrm{PHE}} = R_{\mathrm{P}} \sin 2\varphi$ and φ is the in-plane field azimuthal angle. This result shows that the PHE resistance R_{P} is more than an order of magnitude smaller than the AHE resistance in this system. The determined damping-like effective field $\mu_0 H_{\mathrm{DL}}$ by using Eq. (1) as a function of the applied current I is plotted in fig. S2C. As shown, by increasing the applied current, $\mu_0 H_{\mathrm{DL}}$ also increases linearly. This result demonstrates the existence of the damping-like effective field in the MgO/CoTb/Pt(O) heterostructure.

We also confirmed that the damping-like torque in the MgO/CoTb/Pt(O) heterostructure is independent of the thickness of the semi-insulating Pt(O) layer. We measured the second harmonic AHE resistance $R_{\mathrm{H}}^{2\omega}$ for the MgO/CoTb/Pt(O) heterostructure with $d_{\mathrm{N}} = 9$ nm and 18 nm for $Q = 25\%$ as shown in fig. S4, where d_{N} is the thickness of the Pt(O) layer. The damping-like effective field determined from the $R_{\mathrm{H}}^{2\omega}$ results is $\mu_0 H_{\mathrm{DL}}/I = 0.22$ mT/mA for $d_{\mathrm{N}} = 9$ nm and $\mu_0 H_{\mathrm{DL}}/I = 0.21$ mT/mA for $d_{\mathrm{N}} = 18$ nm. The thickness-independent generation of the spin-orbit torque is consistent with the result obtained from the ST-FMR measurements for the $Ni_{81}Fe_{19}$/Pt(O) bilayer, shown in Fig. 5A in the main text.

section S3. Current-induced magnetization switching

We measured the current-induced magnetization switching for the MgO/CoTb/Pt(O) heterostructures with Q = 20%, 25%, and 30%. We show the AHE resistance R_{H} as a function of a perpendicular magnetic field $\mu_0 H_z$ and a dc charge current I_{dc} for the MgO/CoTb/Pt(O) heterostructures in fig. S5. As shown in R_{H} measured by sweeping the perpendicular magnetic field, the CoTb layer is perpendicularly magnetized in all the MgO/CoTb/Pt(O) devices. Furthermore, we observed the current-induced magnetization switching in all the MgO/CoTb/Pt(O) devices as shown in fig. S5. Although the switching current cannot be compared directly in these devices because of the different magnetic anisotropy of the CoTb layers, this result supports that the damping-like spin-orbit torque large enough to switch the perpendicular magnetization is generated in the heterostructures of ferrimagnetic CoTb sandwiched by the insulating oxides.

section S4. Damping modulation

As an independent check of the validity of the spin-torque efficiency, we also measured the damping modulation for the $SiO_2/Ni_{81}Fe_{19}/Pt(O)$ films with $Q \leq 10\%$ as shown in fig. S6. The damping-like torque efficiency $\xi_{DL} = \mu_0 M_s d_F H_{DL} (2e/\hbar) / {j_c}^{Pt(O)}$ obtained from the damping modulation for the $SiO_2/Ni_{81}Fe_{19}/Pt(O)$ films with $Q = 0$ and 10% is $\xi_{DL} =$ 0.052 and 0.071, respectively, in good agreement with ξ_{DL} obtained from the thickness dependence of the ST-FMR spectra shown in Fig. 4A in the main text.

As shown in Figs. 4C and 5B in the main text, the ratio between the damping-like and field-like spin-orbit torques changes critically by changing Q from 10% to 16%. This discontinuity originates from the disappearance of the bulk contribution to the spin-orbit torques when $Q > 16\%$. As shown in Fig. 2F in the main text, by changing Q from 10% to 16%, the resistivity of the Pt(O) layer is increased more than three-orders of magnitude, despite the small change in Q. Because of the drastic change of the resistivity, the bulk contribution to the spin-orbit torques disappears completely when $Q > 16\%$, which can result in the drastic change in the spin-orbit torques. We also note that the damping-like torque efficiency does not change significantly by increasing Q from 10% to 16%, as evidenced by the damping-modulation measurements. This is supported by the fact that the magnitude of the symmetric component, which is proportional to the damping-like torque, of the ST-FMR spectra does not change significantly with Q as shown in Fig. 2C in the main text. The absence of the drastic change in the damping-like torque indicates that the drastic change of H_{FL}/H_{DL} arises from the negligible field-like torque in the highly oxidized Pt(O) devices.

section S5. Voltage control of spin-orbit torques

In fig. S7, we show a schematic illustration of the fabrication process of the ST-FMR device used for the voltage control of the spin-orbit torques: the $SiO_2/Ni_{81}Fe_{19}/PtO_x/PtO_y/Pt$ heterostructure. In addition to the $SiO_2/Ni_{81}Fe_{19}/PtO_x/PtO_y/Pt$ heterostructure, we also measured the voltage-induced change of the ST-FMR for a SiO_2(4 nm)/$Ni_{81}Fe_{19}$(8 nm)/PtO_y(3.5 nm)/Pt(4 nm) device, where the PtO_x layer is absent (see fig. S8A). Here, the PtO_y layer was fabricated by irradiating accelerated oxygen particles on a Pt film (see also fig. S6). As shown in fig. S8B, we observed the reversible switching of the ST-FMR spectral shape, or the magnitude of S/A, by applying the gate voltages of $\pm$30 V for the $Ni_{81}Fe_{19}/PtO_y/Pt$ device. Although the magnitude and change of S/A cannot be compared directly with the data shown in Fig. 6 in the main text because of the different device structure and microwave frequency, this result supports that the spin-orbit torques can be manipulated by the gate voltage application through the oxygen migration.

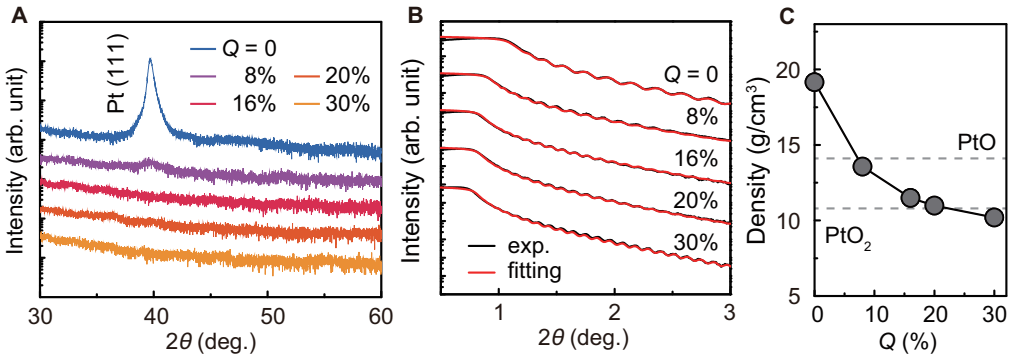

fig. S1. Characterization of Pt(O) films. (**A**) XRD profiles of the Pt(O) films with different Q. (**B**) XRR profiles of the Pt(O) films with different Q. (**C**) Density of the Pt(O) films with different Q obtained from the fitting results of the XRR profiles. The dashed lines indicate the previously reported densities of bulk PtO and PtO_2.

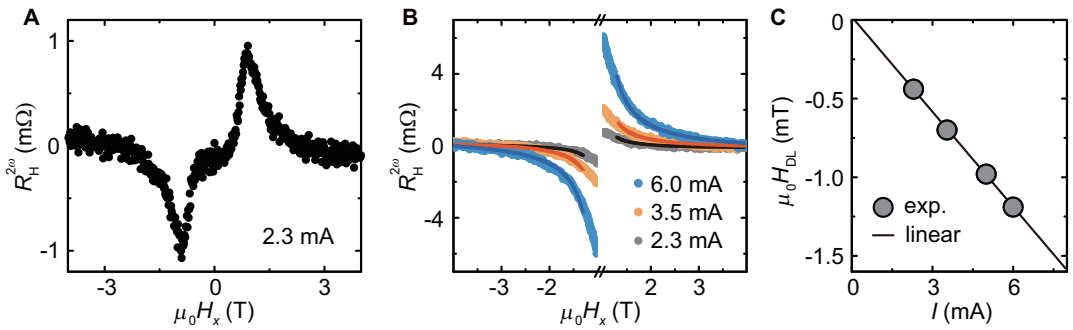

fig. S 2. Second harmonic measurement of the AHE resistance. (**A**) AHE resistance $R_{\mathrm{H}}^{2\omega}$ as a function of an external magnetic field $\mu_0 H_x$ by applying a current of $I = 2.3$ mA. (**B**) Experimental data and fitting results of $R_{\mathrm{H}}^{2\omega}$ by changing the applied current. (**C**) The current induced damping-like effective field $\mu_0 H_{\mathrm{DL}}$ as a function of the applied current I.

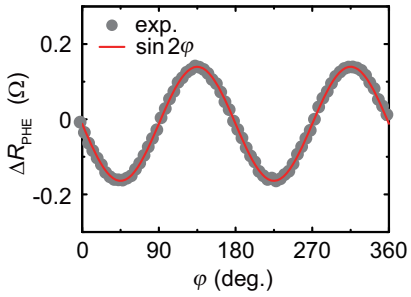

fig. S3. Planar Hall effect resistance. The transverse resistance change ΔR_{PHE} due to the PHE measured for the MgO/CoTb/Pt(O) heterostructure as a function of the field azimuthal angle ϕ of the in-plane external magnetic field.

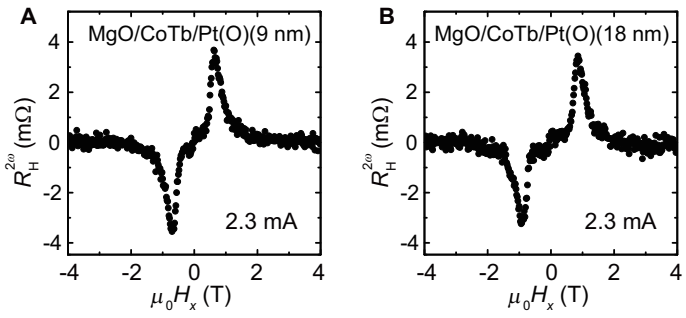

fig. S4. **Pt(O)-layer-thickness dependence of the second harmonic AHE resistance.** The second harmonic AHE resistance $R_{\mathrm{H}}^{2\omega}$ as a function of an external magnetic field $\mu_0 H_x$ by applying a current of $I = 2.3$ mA measured for the perpendicularly-magnetized MgO/CoTb/Pt(O)($Q = 25\%$) heterostructure with (**A**) $d_{\mathrm{N}} = 9$ nm and (**B**) 18 nm.

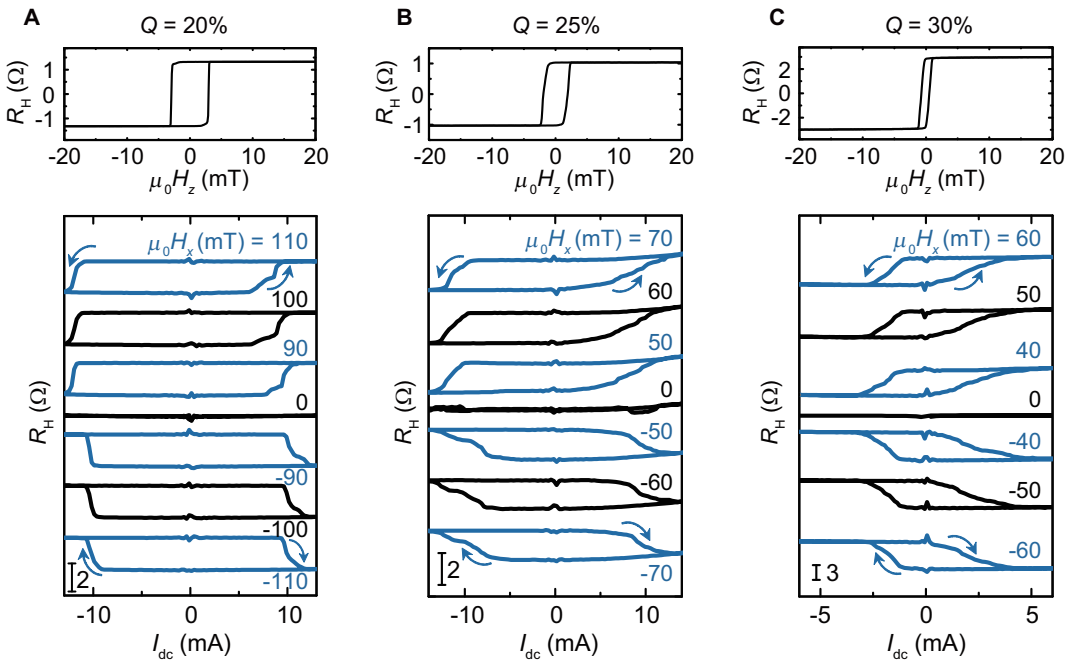

fig. S5. Current-induced magnetization switching. The anomalous Hall resistance R_{H} measured by varying the perpendicular magnetic field $\mu_0 H_z$ and current-induced magnetization switching curves measured with different in-plane external magnetic field $\mu_0 H_x$ for the MgO/CoTb/Pt(O) heterostructures with (**A**) $Q = 20\%$, (**B**) $Q = 25\%$, and (**C**) $Q = 30\%$. The charge current I_{dc} was applied along the x axis for the magnetization switching.

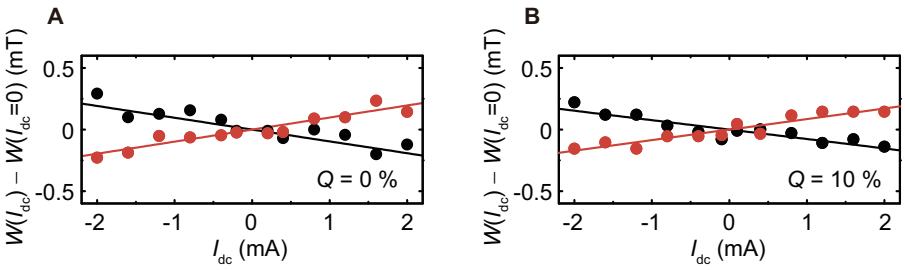

fig. S6. Damping modulation. The change of the linewidth $W(I_{\mathrm{dc}})$ of the ST-FMR spectrum as a function of the applied dc current I_{dc} for the $SiO_2/Ni_{81}Fe_{19}/Pt(O)$ films with (**A**) $Q = 0\%$ and (**B**) $Q = 10\%$.

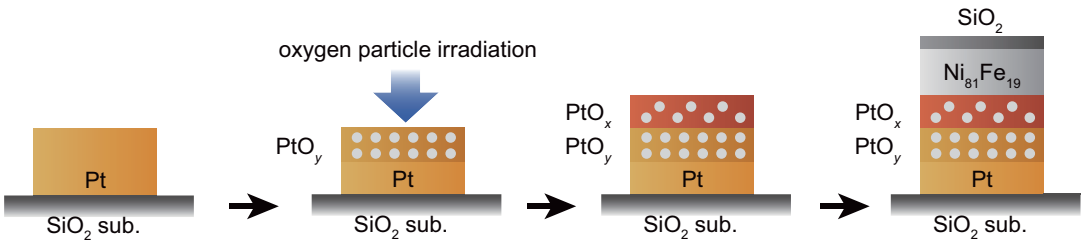

fig. S7. Device fabrication process. A schematic of the fabrication process of the $Ni_{81}Fe_{19}/PtO_x/PtO_y/Pt$ device used for the voltage control of the spin-orbit torques. Firstly, a 7.5-nm-thick Pt layer was sputtered on a SiO_2 substrate, and then accelerated oxygen particles were used to oxidize the Pt film. This oxygen plasma treatment leads to a formation of PtO_y with a depth of around 3.5 nm from the surface. On top of the PtO_y layer, the 7-nm-thick PtO_x layer was sputtered by using the oxygen flow Q of 100% on the PtO_y layer. Finally, the 6-nm-thick $Ni_{81}Fe_{19}$ layer with the 4-nm-thick SiO_2 capping layer was sputtered on the PtO_x layer.

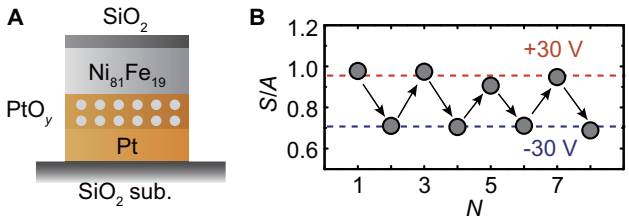

fig. S8. Voltage control of spin-orbit torques. (**A**) Schematic of the $Ni_{81}Fe_{19}/PtO_y/Pt$ device. The gray solid circles represent oxygen ions. (**B**) The magnitude of the S/A ratio measured at 5 GHz, where N represents the cycle index. The ST-FMR were measured for the $Ni_{81}Fe_{19}/PtO_y/Pt$ device after the application of the gate voltage of +30 V ($N = 1, 3, 5, 7$) or −30 V ($N = 2, 4, 6, 8$).